Solar Phys (2014) 289:63–77
DOI 10.1007/s11207-013-0346-0

Preprocessing the Photospheric Vector Magnetograms for an NLFFF Extrapolation Using a Potential-Field Model and an Optimization Method

Chaowei Jiang · Xueshang Feng

Received: 25 December 2012 / Accepted: 7 June 2013 / Published online: 16 July 2013

Abstract Numerical reconstruction/extrapolation of the coronal nonlinear force-free magnetic field (NLFFF) usually takes the photospheric vector magnetogram as input at the bottom boundary. The magnetic field observed at the photosphere, however, contains a force that is in conflict with the fundamental assumption of the force-free model. It also contains measurement noise, which hinders the practical computation. Wiegelmann, Inhester, and Sakurai (*Solar Phys.* **233**, 215, 2006) have proposed to preprocess the raw magnetogram to remove the force and noise to provide better input for NLFFF modeling. In this paper we develop a new code of magnetogram preprocessing that is consistent with our extrapolation method CESE–MHD–NLFFF (Jiang, Feng, and Xiang in *Astrophys. J.* **755**, 62, 2012; Jiang and Feng in *Astrophys. J.* **749**, 135, 2012a). Based on the magnetic-splitting rule that a magnetic field can be split into a potential-field part and a non-potential part, we split the magnetogram and dealt with the two parts separately. The preprocessing of the magnetogram's potential part is based on a numerical potential-field model, and the non-potential part is preprocessed using the similar optimization method of Wiegelmann, Inhester, and Sakurai (2006). The code was applied to the SDO/HMI data, and results show that the method can remove the force and noise efficiently and improve the extrapolation quality.

Keywords Magnetic fields, corona · Magnetic fields, photosphere · Nonlinear force-free field (NLFFF) · Preprocessing

1. Introduction

Magnetic-field extrapolation is an important tool for studying the three-dimensional (3D) solar coronal magnetic field, which is difficult to measure directly (Sakurai, 1989; Aly, 1989; Amari *et al.*, 1997; McClymont, Jiao, and Mikic, 1997; Wiegelmann, 2008; DeRosa *et al.*,

C. Jiang (✉) · X. Feng
SIGMA Weather Group, State Key Laboratory for Space Weather, Center for Space Science and Applied Research, Chinese Academy of Sciences, Beijing 100190, China
e-mail: cwjiang@spaceweather.ac.cn

2009). The models that are most often used for field extrapolation are the potential-field model, the linear force-free-field model, and the nonlinear force-free-field (NLFFF) model. These models are all based on the assumption that the Lorentz force is self-balancing in the corona, but they adopt different simplifications of the current distribution. Among these models, the NLFFF model is the most precise one for characterizing magnetic field in the low corona, where there is significant and localized electric current, especially in active regions.

It is routine to use the vector magnetograms observed on the photosphere as input for the NLFFF extrapolation, at least in most of the available extrapolation codes (*e.g.*, Wheatland, Sturrock, and Roumeliotis, 2000; Wiegelmann, 2004; Amari, Boulmezaoud, and Aly, 2006; Valori, Kliem, and Fuhrmann, 2007; Jiang and Feng, 2012a; Jiang, Feng, and Xiang, 2012; Inoue *et al.*, 2011).[1] This poses a basic problem (and also a major headache) to the force-free-field modelers, however, because the magnetic field in the photosphere is significantly forced by the plasma (Metcalf *et al.*, 1995), which is in conflict with the fundamental assumption of force-freeness. From the photosphere to the corona, the magnetic field passes through a highly stratified and inhomogeneous plasma environment with plasma β varying abruptly from >1 to $\ll 1$ (Gary, 2001); thus the force-free condition cannot be fulfilled globally. By studying the observed chromospheric field in a sampled active region, Metcalf *et al.* (1995) concluded that the magnetic field is not force-free in the photosphere, but becomes force-free roughly 400 km above the photosphere. A recent statistical study by Liu *et al.* (2013) using a large number of magnetograms from Huairou Solar Observing Station arrived at similar conclusions.

This complication leads to the desire to use measurements of the vector field in the force-free upper chromosphere instead. However, the vector field is not as easily measured in the chromosphere as in the photosphere. Even if the chromospheric field is measured, it is still challenging to extrapolate it since the surface on which any particular magnetically sensitive line will form varies in time and space, and in particular the height will be different along different lines of sight. Therefore one cannot assume that the vector field is given on a plane or sphere at the bottom of the extrapolation volume, as for the photospheric magnetograms. The practical use of the chromospheric magnetograms as boundary conditions for extrapolations is still to be explored.

As an alternative way to alleviate the problem, one can consider modifying the photospheric magnetograms to simulate the force-free chromospheric magnetograms, which was first suggested by Wiegelmann, Inhester, and Sakurai (2006). Since the interface between the photosphere and the bottom of the force-free domain is very thin (about 400 km), especially when compared with the spatial scale of the coronal field (about tens of megameters), the basic field-structures of the chromosphere are probably very similar to those of the photosphere, except that i) there must be some smoothness of the structures due to the fast expansion of field from the high-β to low-β regions, and ii) the very fine magnetic elements are just closed within this interface and thus show no signal in the force-free domain. Therefore, modifications that need to be made on the photospheric field to mimic the force-free chromospheric field ought to be insignificant and can hopefully be made within or at about the error margins of the measurement.

[1] There are also some NLFFF models that use only the line-of-sight component of the photospheric field, along with constraints from other observed information such as the EUV loops, filament channels, and X-ray sigmoid structure (*e.g.*, Bobra, van Ballegooijen, and DeLuca, 2008; Su *et al.*, 2009; Aschwanden *et al.*, 2012).

The procedure of modifying a raw photospheric magnetogram to a force-free chromospheric one is called preprocessing (Wiegelmann and Neukirch, 2006; Fuhrmann, Seehafer, and Valori, 2007; Metcalf *et al.*, 2008; Fuhrmann *et al.*, 2011; Yamamoto and Kusano, 2012). To guide the preprocessing, there are constraints that must be fulfilled by the target magnetogram. On the boundary surface S of an ideally force-free field $\mathbf{B}$ in a volume V, the field satisfies the following necessary conditions[2]

$$\begin{aligned} F_x &= \int_S B_x B_z \,\mathrm{d}x\,\mathrm{d}y = 0, \qquad F_y = \int_S B_y B_z \,\mathrm{d}x\,\mathrm{d}y = 0, \\ F_z &= \int_S E_B \,\mathrm{d}x\,\mathrm{d}y = 0, \qquad T_x = \int_S y E_B \,\mathrm{d}x\,\mathrm{d}y = 0, \qquad T_y = \int_S x E_B \,\mathrm{d}x\,\mathrm{d}y = 0, \\ T_z &= \int_S (y B_x B_z - x B_y B_z) \,\mathrm{d}x\,\mathrm{d}y = 0, \end{aligned} \tag{1}$$

where $E_B = B_x^2 + B_y^2 - B_z^2$. These expressions are derived from the volume integrals of the total magnetic force and torque (Aly, 1989; Sakurai, 1989; Tadesse, 2011)

$$\begin{aligned} \mathbf{0} &= \int_V \mathbf{j} \times \mathbf{B} \,\mathrm{d}V = \int_V \nabla \cdot \mathbf{T} \,\mathrm{d}V = \int_S \mathbf{T} \,\mathrm{d}\mathbf{S}, \\ \mathbf{0} &= \int_V \mathbf{r} \times (\mathbf{j} \times \mathbf{B}) \,\mathrm{d}V = \int_V \nabla \cdot \mathbf{T}' \,\mathrm{d}V = \int_S \mathbf{T}' \,\mathrm{d}\mathbf{S}, \end{aligned} \tag{2}$$

where $\mathbf{T}$ is magnetic stress tensor

$$\mathbf{T}_{ij} = -\frac{\mathbf{B}^2}{2}\delta_{ij} + B_i B_j \tag{3}$$

and $\mathbf{T}'_{ij} = \epsilon_{ikl} r_k \mathbf{T}_{lj}$. Generally, the surface integration has to be carried out over a closed volume, but in preprocessing magnetograms to extrapolate a computational cube, the surface integrals of Equation (2) are usually restricted within the bottom magnetogram since the contribution from other (side and top) boundaries is small and negligible, and in the following S will represent only the area of magnetograms. With this assumption, Equation (1) is the component form of the surface integrals in Equation (2). The first task of preprocessing accordingly is to drive the raw magnetogram to fulfill the constraints of Equation (1) and thus to be closer to an ideally force-free magnetogram. This task is also dubbed removing the force in the forced magnetogram. The second task of preprocessing is to smooth the raw data to mimic the field expansion. Smoothing is also very necessary for the practical computation based on the numerical difference with the limited resolution, which cannot resolve small enough structures in the raw data. In addition, smoothing can remove measurement noise and increase the signal-to-noise ratio.

Several preprocessing codes (Wiegelmann, Inhester, and Sakurai, 2006; Fuhrmann, Seehafer, and Valori, 2007; Metcalf *et al.*, 2008) have been developed. They share the basic approach proposed by Wiegelmann, Inhester, and Sakurai (2006). A functional L is designed by summing the χ^2 deviations from the constraints of Equation (1), the terms that control the deviation from the raw data and the smoothness with different weights, *e.g.*,

$$L = \mu_1 L_1 + \mu_2 L_2 + \mu_3 L_3 + \mu_4 L_4, \tag{4}$$

[2]The necessary conditions mean that even fulfilling these conditions, the magnetogram may still contain force; but magnetograms that fulfill these conditions are certainly better input for the NLFFF model than those that do not.

where μ is the weighting factor, $L_1 = F_x^2 + F_y^2 + F_z^2$, $L_2 = T_x^2 + T_y^2 + T_z^2$, $L_3 = \int_S |\mathbf{B} - \mathbf{B}_{\rm obs}|^2 \, {\rm d}s$, and L_4 measures the roughness of the data. Then the target magnetogram is searched by minimizing the functional L using an optimization method. Different algorithms of smoothing and optimization have been used and the results are more or less different, as shown in a comparison study by Fuhrmann *et al.* (2011). The differences can also result from different choices of the weighting factors.

Within this framework of preprocessing, two problems are only poorly addressed, namely, to what extent the force needs to be removed and to what extent the smoothing can be performed. We consider these problems from both numerical and physical points of view. Ideally, we prefer the map to satisfy the force-free constraints precisely, but this condition need not be so strictly satisfied because a numerical discretization error is unavoidable in an extrapolation with finite resolution. The smoothing also ought not to be made arbitrarily if we aim to mimic the expansion of the field from the photosphere to some specific height above. Too much smoothing of the data may smear the basic structures while too little smoothing cannot filter the small-scale noise sufficiently. A careful choice of the weighting factors μ is required to deal with these problems.

This paper is devoted to handling these problems in the preprocessing. We used the values of force-freeness and smoothness calculated from a numerical potential-field solution at some height above the photosphere as a reference to guide the preprocessing. Based on the simple rule that any magnetic field can be split into two parts, a potential field and a non-potential field, we developed a new preprocessing code using this magnetic-field splitting that is consistent with our extrapolation code CESE–MHD–NLFFF (Jiang and Feng, 2012a; Jiang, Feng, and Xiang, 2012). We show below how the raw magnetogram can be driven to be force-free and smooth with the same level as that of the numerical potential field at a height of roughly 400 km above the photosphere, *i.e.*, the bottom of the force-free domain. The remainder of the paper is organized as follows. In Section 2 we give the basic method and formulas and show how the weighting factors are chosen in Section 3. We then apply the method to preprocess two sampled magnetograms taken by SDO/HMI and analyze the results in Section 4. Finally, discussion and conclusions are given in Section 5.

2. Method

Generally, the coronal magnetic field can be split into two parts: a potential field matching the normal component of the bottom magnetogram, and a non-potential part with the normal field vanishing at the bottom. Particularly, for the vector magnetogram, the magnetic field $\mathbf{B}$ can be written as

$$\mathbf{B} = \mathbf{B}_0 + \mathbf{B}_1 = (B_{0x} + B_{1x}, B_{0y} + B_{1y}, B_{0z}), \tag{5}$$

where (B_{0x}, B_{0y}, B_{0z}) are the components of the potential part $\mathbf{B}_0$ and (B_{1x}, B_{1y}) are the components of the non-potential part $\mathbf{B}_1$. Note that $B_{0z} = B_z$ and $B_{1z} = 0$.

Assuming that $\mathbf{B}$ is a force-free magnetogram, and because its potential part $\mathbf{B}_0$ already fulfills the force-free conditions of Equation (1), we can derive special force-free conditions for its non-potential part (B_{1x}, B_{1y}), which are expressed as

$$\begin{aligned}
&\int_S B_{1x} B_{0z} \, {\rm d}x \, {\rm d}y = 0, \qquad \int_S B_{1y} B_{0z} \, {\rm d}x \, {\rm d}y = 0, \\
&\int_S \Gamma_B \, {\rm d}x \, {\rm d}y = 0, \qquad \int_S x \Gamma_B \, {\rm d}x \, {\rm d}y = 0, \qquad \int_S y \Gamma_B \, {\rm d}x \, {\rm d}y = 0, \\
&\int_S (y B_{1x} B_{0z} - x B_{1y} B_{0z}) \, {\rm d}x \, {\rm d}y = 0,
\end{aligned} \tag{6}$$

where we denote $\Gamma_B = B_{1x}^2 + B_{1y}^2 + 2(B_{0x}B_{1x} + B_{0y}B_{1y})$. The derivation is straightforward, for example

$$\begin{aligned} E_B &= (B_{0x} + B_{1x})^2 + (B_{0y} + B_{1y})^2 - B_{0z}^2 \\ &= E_{B_0} + B_{1x}^2 + B_{1y}^2 + 2(B_{0x}B_{1x} + B_{0y}B_{1y}) = E_{B_0} + \Gamma_B, \end{aligned} \tag{7}$$

and we have

$$\int_S \Gamma_B \, \mathrm{d}x \, \mathrm{d}y = \int_S E_B \, \mathrm{d}x \, \mathrm{d}y - \int_S E_{B_0} \, \mathrm{d}x \, \mathrm{d}y = 0. \tag{8}$$

All other expressions in Equation (6) can be derived easily in a similar way.

Let $\mathcal{B}$ $(\mathcal{B}_x, \mathcal{B}_y, \mathcal{B}_z)$ denote the observed photospheric field, *i.e.*, the raw magnetogram, and its splitting form is

$$\mathcal{B} = \mathcal{B}_0 + \mathcal{B}_1 = (\mathcal{B}_{0x} + \mathcal{B}_{1x}, \mathcal{B}_{0y} + \mathcal{B}_{1y}, \mathcal{B}_{0z}), \tag{9}$$

with $\mathcal{B}_0$ and $\mathcal{B}_1$ denoting the potential and non-potential parts, respectively. Here $\mathcal{B}_0$ is computed based on $\mathcal{B}_z$ using the potential-field model, and from this $\mathcal{B}_1$ is obtained. The computation of a potential field needs only the normal component of the field on the bottom and is now a trivial task, which can be carried out conveniently by using the Green's function method (Metcalf *et al.*, 2008) or other much faster schemes (Jiang and Feng, 2012b).

Generally, $\mathcal{B}_1$ does not fulfill the force-free conditions of Equation (6). For the case without smoothing, we only need to let $\mathbf{B}_0 = \mathcal{B}_0$ and reduce the non-potential part $\mathcal{B}_1$ to $\mathbf{B}_1$ to satisfy Equation (6). For the purpose of smoothing, $\mathbf{B}_0$ is obtained by taking the data at a plane just one pixel above the photosphere from the 3D potential field extrapolated from the observed $\mathcal{B}_{0z}$. This is suitable for the SDO/HMI data, which have a pixel size of about 360 km (*i.e.*, 0.5 arcsec), an approximate height above which the coronal field becomes force-free according to Metcalf *et al.* (1995). For magnetograms with other pixel sizes, we need to take the potential field data at a given physical height (where the force-free assumption becomes valid, *e.g.*, 400 km) and not necessarily one pixel above the photosphere. The potential part $\mathbf{B}_0$ obtained in this way can be regarded as the potential part of the chromospheric field, also a preprocessed counterpart of $\mathcal{B}_0$. Of course, if measurements of chromospheric longitudinal fields are available (*e.g.*, Yamamoto and Kusano, 2012), we recommend using these data directly to construct the potential part $\mathbf{B}_0$, which is certainly preferred over that based on the photospheric $\mathcal{B}_{0z}$.

The second task, reducing $\mathcal{B}_1$ to $\mathbf{B}_1$, is carried out using an optimization method similarly to Wiegelmann, Inhester, and Sakurai (2006). We intend to minimize the total magnetic force and torque, which are quantified by

$$L_1 = L_{11}^2 + L_{12}^2 + L_{13}^2, \qquad L_2 = L_{21}^2 + L_{22}^2 + L_{23}^2, \tag{10}$$

where for convenience of presentation we denote

$$L_{11} \equiv \sum_{\mathrm{p}} B_{1x}B_{0z}, \qquad L_{12} \equiv \sum_{\mathrm{p}} B_{1y}B_{0z}, \qquad L_{13} \equiv \sum_{\mathrm{p}} \Gamma_B, \tag{11}$$

$$L_{21} \equiv \sum_{\mathrm{p}} x\Gamma_B, \qquad L_{22} \equiv \sum_{\mathrm{p}} y\Gamma_B, \qquad L_{23} \equiv \sum_{\mathrm{p}} (yB_{1x}B_{0z} - xB_{1y}B_{0z}). \tag{12}$$

Here the summation $\sum_{\mathrm{p}}$ is over all the pixels of the magnetogram, and these summations are the numerical counterparts of the integrals in Equation (6).

The observation term L_3 (to restrict the deviation from the observed data) and the smoothing functional L_4 (to control the smoothness) are also considered by Wiegelmann, Inhester, and Sakurai (2006),

$$
\begin{aligned}
L_3 &= \sum_{\mathrm{p}} \left[(B_{1x} - \mathcal{B}_{1x})^2 + (B_{1y} - \mathcal{B}_{1y})^2 \right], \\
L_4 &= \sum_{\mathrm{p}} \left[(\Delta B_{1x})^2 + (\Delta B_{1y})^2 \right],
\end{aligned}
\tag{13}
$$

where Δ is a common five-point 2D-Laplace operator, *i.e.*, for the pixel (i, j)

$$
\Delta B_{i,j} \equiv B_{i+1,j} + B_{i-1,j} + B_{i,j+1} + B_{i,j-1} - 4B_{i,j}. \tag{14}
$$

This simply states that the smaller L_4, the smoother the data.

Additionally, the above functionals L_ℓ (where $\ell = 1, 2, 3, 4$) are normalized by N_ℓ, which are given by

$$
\begin{aligned}
N_1 &= \left(\sum_{\mathrm{p}} |\mathcal{B}|^2 \right)^2, \qquad & N_2 &= \left(\sum_{\mathrm{p}} \sqrt{x^2 + y^2} |\mathcal{B}|^2 \right)^2, \\
N_3 &= \sum_{\mathrm{p}} \left(\mathcal{B}_x^2 + \mathcal{B}_y^2 \right), \qquad & N_4 &= \sum_{\mathrm{p}} \left[(\overline{\Delta} \mathcal{B}_{1x})^2 + (\overline{\Delta} \mathcal{B}_{1y})^2 \right],
\end{aligned}
\tag{15}
$$

where

$$
\overline{\Delta} B_{i,j} \equiv B_{i+1,j} + B_{i-1,j} + B_{i,j+1} + B_{i,j-1} + 4B_{i,j}. \tag{16}
$$

We used the steepest-descent method (Press *et al.*, 1992) to minimize the weighted average of the above functionals,

$$
L = \sum_{\ell=1}^{4} \frac{\mu_\ell}{N_\ell} L_\ell, \tag{17}
$$

where μ_ℓ is the weighting factor. Generally, the weighting factors for the magnetic force and torque are simply given by $\mu_1 = \mu_2 = 1$ since there is no obvious reason for a bias on one of these two quantities. The determination of μ_3 and μ_4 is described in the next section, and different combinations of them are tested for two HMI magnetograms to search for the best choice in Section 4.

Since L is an explicit functional of the arguments (B_{1x}, B_{1y}), its gradient ∇L can be expressed at each pixel q as

$$
\begin{aligned}
\frac{\partial L}{\partial (B_{1x})_q} &= 2 \frac{\mu_1}{N_1} \left[L_{11} (B_{0z})_q + L_{13} (2B_{1x} + 2B_{0x})_q \right] \\
&\quad + 2 \frac{\mu_2}{N_2} \left[L_{21} (2x B_{1x} + 2x B_{0x})_q + L_{22} (2y B_{1x} + 2y B_{0x})_q + L_{23} (y B_{0z})_q \right] \\
&\quad + 2 \frac{\mu_3}{N_3} (B_{1x} - \mathcal{B}_{1x})_q + 2 \frac{\mu_4}{N_4} \left(\Delta (\Delta B_{1x}) \right)_q,
\end{aligned}
\tag{18}
$$

$$
\begin{aligned}
\frac{\partial L}{\partial (B_{1y})_q} &= 2 \frac{\mu_1}{N_1} \left[L_{12} (B_{0z})_q + L_{13} (2B_{1y} + 2B_{0y})_q \right] \\
&\quad + 2 \frac{\mu_2}{N_2} \left[L_{21} (2x B_{1y} + 2x B_{0y})_q + L_{22} (2y B_{1y} + 2y B_{0y})_q + L_{23} (-x B_{0z})_q \right] \\
&\quad + 2 \frac{\mu_3}{N_3} (B_{1y} - \mathcal{B}_{1y})_q + 2 \frac{\mu_4}{N_4} \left(\Delta (\Delta B_{1y}) \right)_q.
\end{aligned}
\tag{19}
$$

The procedure of the steepest descent is performed as follows. We start from an initial guess (B_{1x}^0, B_{1y}^0), *e.g.*, the observed data $(\mathcal{B}_{1x}, \mathcal{B}_{1y})$, and march the solution in each iteration k along the steepest-descent direction (*i.e.*, opposite to the gradient direction) by

$$
\left(B_{1x}^{k+1} \right)_q = \left(B_{1x}^k \right)_q - \lambda_k \frac{\partial L}{\partial (B_{1x}^k)_q}, \qquad \left(B_{1y}^{k+1} \right)_q = \left(B_{1y}^k \right)_q - \lambda_k \frac{\partial L}{\partial (B_{1y}^k)_q}. \tag{20}
$$

It is important to choose a proper step size λ_k at each step to maximize the local descent. This can be determined by a bisection line-search algorithm to solve the one-dimensional optimization problem at every iteration

$$\lambda_k = \arg\min L\left(\mathbf{B}_1^k - \lambda \nabla L\left(\mathbf{B}_1^k\right)\right). \tag{21}$$

The iteration is terminated if the maximum residual of the field $[\mathrm{res}(\mathbf{B}_1)]_{\max}$, defined by

$$\left[\mathrm{res}(\mathbf{B}_1)\right]_{\max} = \lambda_k \max\left[\nabla L\left(\mathbf{B}_1^k\right)\right], \tag{22}$$

is smaller than 0.1 gauss (G) for ten successive steps.

3. Choice of the Weighting Factor μ

A careful choice of the best weighting factors μ is critical for a good performance of the preprocessing. Using the qualities of force-freeness and smoothness of the numerical potential part $\mathbf{B}_0$ as a reference, we guide the optimization of μ according to the follow constraints:

i) The residual force and torque in the target magnetogram $\mathbf{B}$ should be reduced to the same order as those in $\mathbf{B}_0$.
ii) The smoothness of the target magnetogram $\mathbf{B}$ should reach the same level as that of $\mathbf{B}_0$ (since $B_z = B_{0z}$, the smoothness of B_x and B_y should match that of B_z. This is reasonable since there is no preference for any component of the vector).
iii) With the constraints i) and ii) fulfilled, the deviation between the target magnetogram $\mathbf{B}$ and the observed data $\mathcal{B}$ should be minimized.

Within the constraints the residual magnetic force and torque of the data are quantified by two parameters, $\epsilon_{\mathrm{force}}$ and $\epsilon_{\mathrm{torque}}$, defined as usual

$$\epsilon_{\mathrm{force}} = \frac{|\sum_{\mathrm{p}} B_x B_z| + |\sum_{\mathrm{p}} B_y B_z| + |\sum_{\mathrm{p}} E_B|}{\sum_{\mathrm{p}} (B_x^2 + B_y^2 + B_z^2)}, \tag{23}$$

$$\epsilon_{\mathrm{torque}} = \frac{|\sum_{\mathrm{p}} x E_B| + |\sum_{\mathrm{p}} y E_B| + |\sum_{\mathrm{p}} (y B_x B_z - x B_y B_z)|}{\sum_{\mathrm{p}} \sqrt{x^2 + y^2}(B_x^2 + B_y^2 + B_z^2)}, \tag{24}$$

and the smoothness of component B_m ($m = x, y, z$) is measured by

$$S_m = \sum_{\mathrm{p}} \left[(\Delta B_m)^2\right] / \sum_{\mathrm{p}} \left[(\overline{\Delta} B_m)^2\right]. \tag{25}$$

In addition to these constraints the total iteration steps needed for the computation are also considered if the magnetogram's resolution is very high, since the computing time of the preprocessing may be very long.

4. Preprocessing the SDO/HMI Magnetograms

In this section we apply the preprocessing code to several magnetograms taken by SDO/HMI, and search for the best values for the weighting factors. The *Helioseismic and Magnetic Imager* (HMI) onboard the *Solar Dynamics Observatory* (SDO) provides photospheric vector magnetograms with a high resolution in space and time. It observes the full Sun with a 4k×4k CCD whose spatial sampling is 0.5 arcsec per pixel. Raw filtergrams are

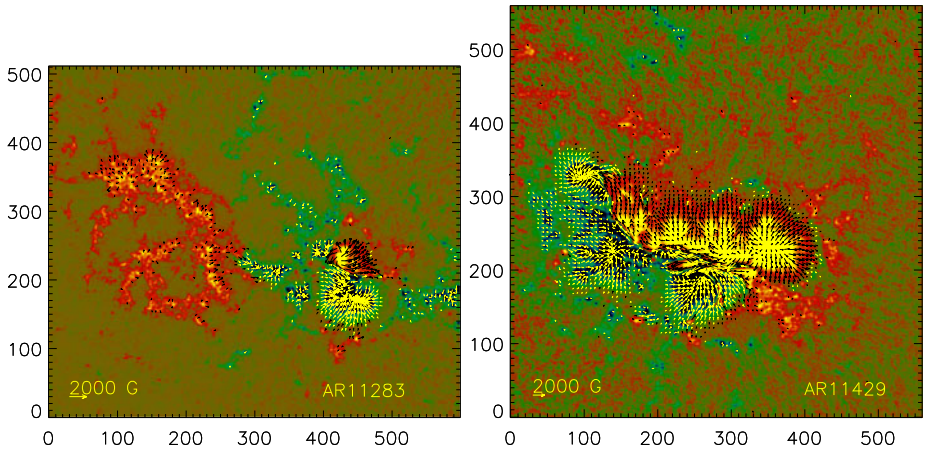

Figure 1 The observed vector magnetograms for AR 11283 at 05:36 UT on 8 September 2011 and AR 11429 at 00:00 UT on 7 March 2012. The background shows the vertical components with saturation values of ± 1000 G; the vectors represent the transverse field, and only the field stronger than 200 G is plotted. The length unit is 0.5 arcsec.

obtained at six different wavelengths and six polarization states in the Fe I 6173 Å absorption line, and are collected and converted to observable quantities (such as Dopplergrams, continuum filtergrams, and line-of-sight and vector magnetograms) on a rapid time cadence. For the vector magnetic data, each set of filtergrams takes 135 s to be completed. To obtain vector magnetograms, Stokes parameters are first derived from filtergrams observed over a 12-min interval and are then inverted through Very Fast Inversion of the Stokes Vector (VFISV; Borrero *et al.*, 2011). The 180° azimuthal ambiguity in the transverse field is resolved by an improved version of the minimum-energy algorithm (Leka *et al.*, 2009). Regions of interest with a strong magnetic field are automatically identified near real time (Turmon *et al.*, 2010). A detailed description on how the vector magnetograms are produced can be found on the website http://jsoc.stanford.edu/jsocwiki/VectorPaper.

The raw magnetograms we used here were downloaded from http://jsoc.stanford.edu/jsocwiki/ReleaseNotes2, where the HMI vector magnetic field data series `hmi.B_720s_e15w1332` are released for several active regions. There are two special formats, direct cutouts and remapped images. We used the remapped format, which is more suitable for modeling in local Cartesian coordinates, since the images are computed with a Lambert cylindrical equal-area projection centered on the tracked region. For our test, we selected two active regions, AR 11283 and AR 11429, both of which produced X-class flares and thus were very non-potential. Figure 1 shows the magnetograms for AR 11283 at 05:36 UT on 8 September 2011 and AR 11429 at 00:00 UT on 7 March 2012. The size of the magnetograms are 600×512 and 560×560 pixels, respectively.

In Figures 2 and 3 we show the preprocessing results with different sets of μ_3 and μ_4. Since for such large magnetograms it is challenging to perform many tests with continuous sets of weighting factors to pick the optimal factor, we only computed the results for several groups of μ_3 and μ_4 as shown in the figures, *i.e.*, $\mu_3 = 1, 0.1, 0.01, 0.001, 0.0001$, and $\mu_4 = 1, 0.1, 0.01, 0.001$. For each set of weighting factors, the normalized terms L_l/N_l, the smoothness, and the force-free quality ϵ_{force} and ϵ_{torque} are plotted. By comparing the results with fixed μ_3 but different μ_4, we can see that the force-free parameters L_1/N_1, L_2/N_2, ϵ_{force}, and ϵ_{torque} are almost entirely determined by μ_3. When decreasing μ_3,

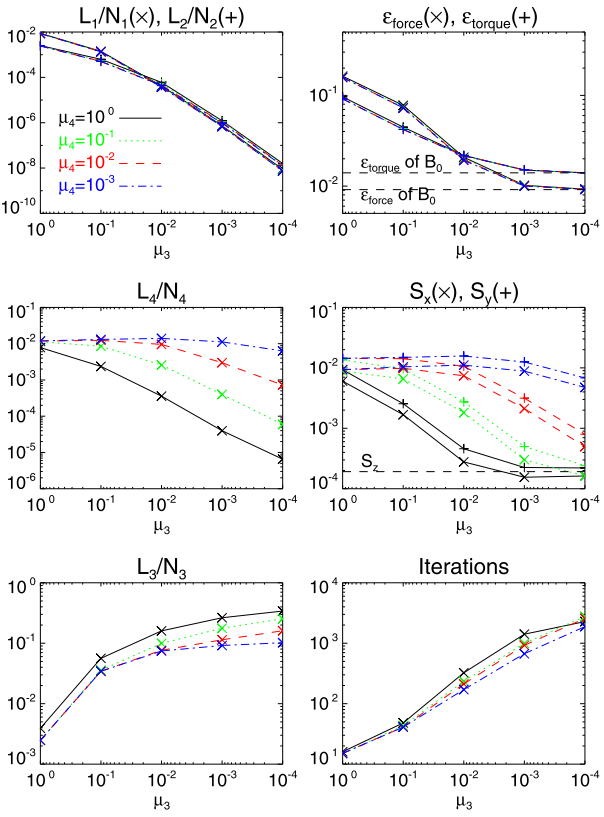

Figure 2 Preprocessed results for the magnetogram of AR 11283 with different μ_3 and μ_4. Results for different values of μ_4 are plotted using different colors and line styles, as denoted in the top left panel. The dashed lines in the top right and middle right panels represent the parameter values of the potential part $\mathbf{B}_0$, which is used as the reference to choose the optimal weights. They are chosen such that ϵ_{force}, ϵ_{torque}, S_x, and S_y are close to those of $\mathbf{B}_0$, and L_3/N_3 is minimized.

i.e., allowing more freedom of modifying the raw data, L_1 and L_2 decrease very quickly (their magnitude decreases quicker than that of μ_3), but the residual force parameters ϵ_{force} and ϵ_{torque} reach a minimum and cannot be reduced any further. This is because the potential part $\mathbf{B}_0$ has a non-zero value of ϵ_{force} and ϵ_{torque} (because of the numerical error of the finite resolution), which is the minimum of ϵ_{force} and ϵ_{torque} that can be reached for the target magnetograms. The results for both tests show that $\mu_3 = 0.001$ is small enough, which gives ϵ_{force} and ϵ_{torque} nearly the same as those of $\mathbf{B}_0$, meaning that the force in the non-potential part $\mathbf{B}_1$ is decreased near to, or below, the level of numerical error. Even smaller μ_3 cannot improve the quality of force-freeness, but deviates the target magnetograms farther away from the original data. Accordingly, we set the optimal value as $\mu_3 = 0.001$. With a given value of μ_3, the smoothness values are controlled by μ_4. Obviously, $\mu_4 = 1$ is a good choice, which yields values of S_x and S_y very similar to S_z, meaning that the smoothness of the target magnetograms is consistent with their potential part $\mathbf{B}_0$. Our choice of the smoothness weight is more physically correct than what has been assumed in other methods, for which it has been given more or less arbitrarily.

The results of preprocessing the two magnetograms with the optimal weighting factors $\mu_3 = 0.001$ and $\mu_4 = 1$ are summarized in Table 1. Figures 4 and 5 show a comparison of the original and preprocessed magnetograms. Here the color-map is designed to manifest both strong and weak fields. As shown, the map after preprocessing resamples the feature of the original data, while small structures tend to be smoothed out. In the bottom of the

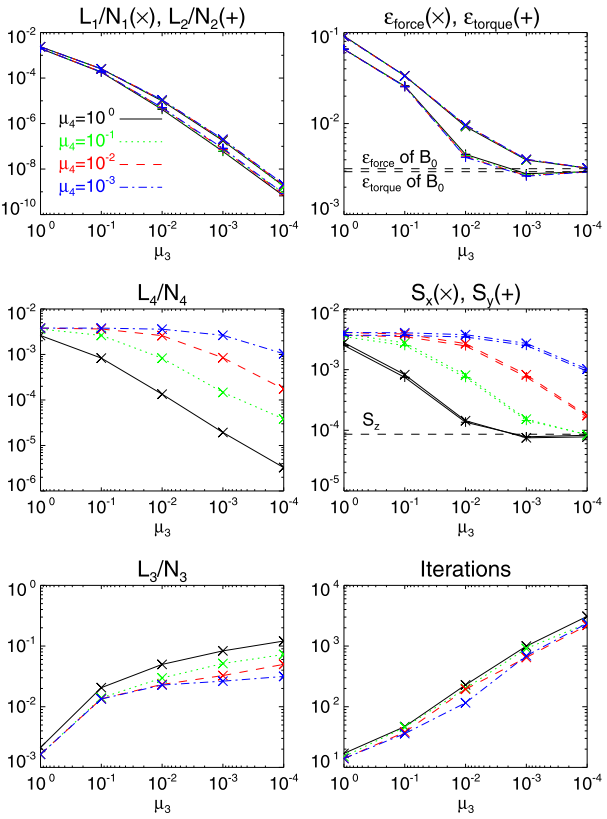

Figure 3 Same as Figure 2, but for AR 11429.

Table 1 Quality of the magnetograms. The preprocessed results are produced with the optimal weighting factors $\mu_3 = 0.001$ and $\mu_4 = 1$. The parameter ϵ_{flux} is the total magnetic flux normalized by the total unsigned flux.

Data	ϵ_{flux}	ϵ_{force}	ϵ_{torque}	S_x	S_y	S_z
AR 11283						
Raw	−7.88E–02	2.84E–01	2.38E–01	8.38E–03	1.28E–02	2.49E–03
Preprocessed	−8.98E–02	1.02E–02	1.50E–02	1.55E–04	2.25E–04	1.92E–04
Numerical potential	−8.98E–02	9.14E–03	1.40E–02	2.10E–04	1.78E–04	1.92E–04
AR 11429						
Raw map	−1.36E–02	1.82E–01	1.55E–01	3.76E–03	3.43E–03	1.21E–03
Preprocessed map	−1.46E–02	3.98E–03	2.81E–03	7.52E–05	7.82E–05	8.61E–05
Numerical potential	−1.46E–02	3.19E–03	2.96E–03	8.38E–05	8.53E–05	8.61E–05

figures we plot the results for the vertical current J_z, which was calculated by taking finite differences of the transverse field

$$J_z^{i,j} = \frac{B_y^{i+1,j} - B_y^{i-1,j}}{2} - \frac{B_x^{i,j+1} - B_x^{i,j-1}}{2}. \tag{26}$$

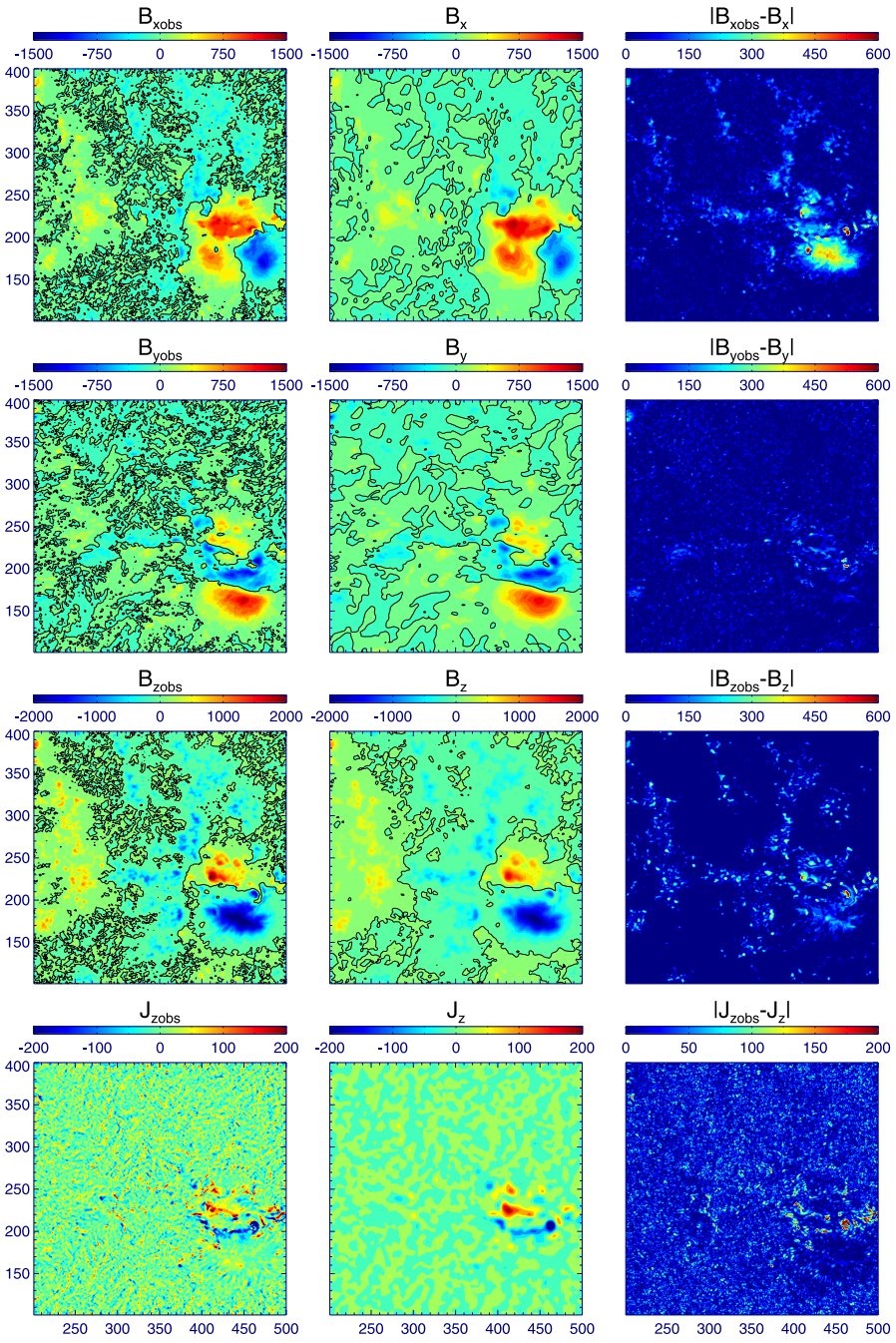

Figure 4 Comparison of the raw magnetogram and preprocessed magnetogram for AR 11283. The left column lists the raw data, the middle column the preprocessed data, and the right column shows the absolute differences between them. Rows from top to bottom are the three components of the data and the vertical current J_z, respectively. On the images of the B_x, B_y, and B_z components are plotted the contour lines of their zero values.

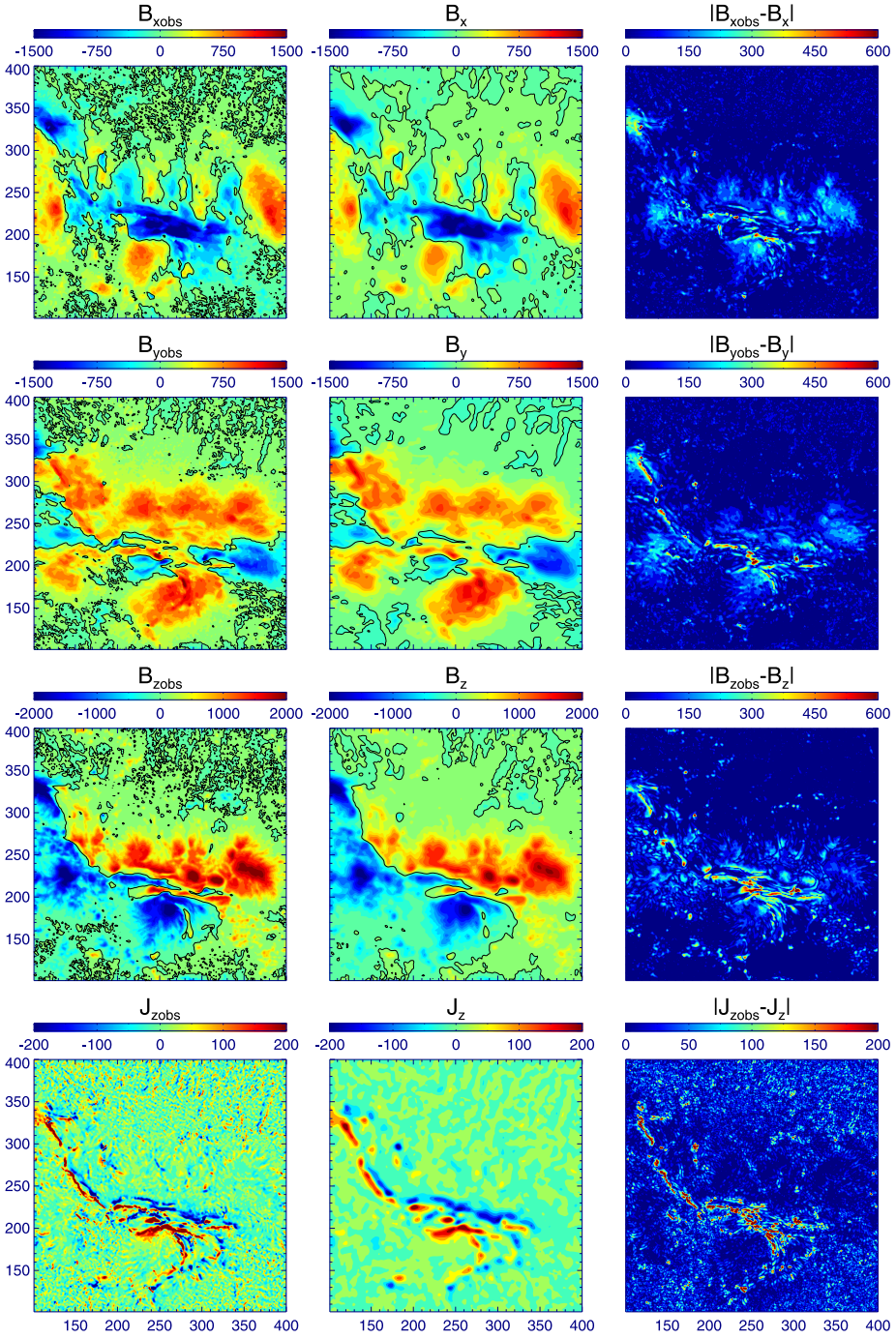

Figure 5 Same as Figure 4, but for AR 11429.

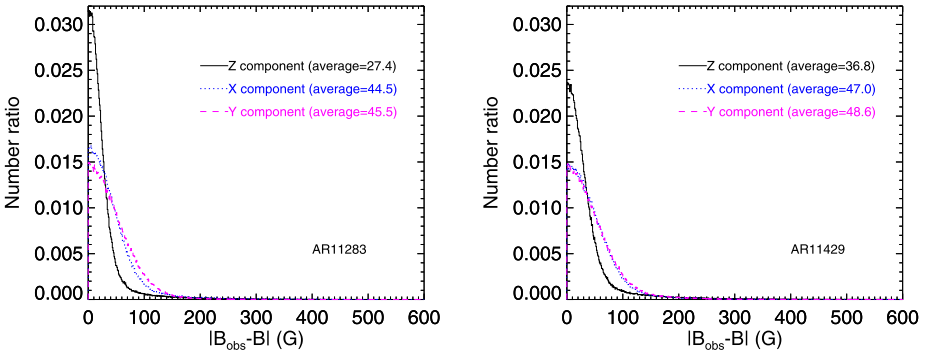

Figure 6 Histograms of the changes of the vector components for all the pixels between the raw and preprocessed magnetograms. The horizontal axis represents the absolute values of the differences between the raw and preprocessed data, the vertical axis represents the number of the pixels normalized by the total number. The average changes are also labeled in the figure.

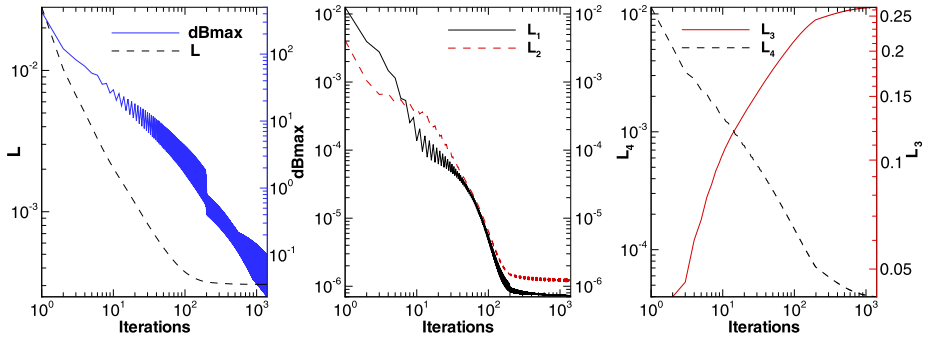

Figure 7 Evolutions of the functional with iterations in the optimization process. dBmax is the maximum residual of the field in each iteration step, see Equation (22).

Since the numerical differences are very sensitive to noise, random noise in the data appears more clearly in the J_z map, particularly in weak-field regions, and they are suppressed effectively by the smoothing. Histograms are plotted in Figure 6 to show the distributions of the absolute differences between the raw and preprocessed magnetograms over all the pixels. Apparently, different approaches of modifying the data give different distributions, *i.e.*, the distribution for the z-component is distinct from those for the x- and y-components. This is because the modification for B_z is determined solely by the potential model, while modifications for B_x, B_y are additionally made by the optimization process. The change in the vertical field is less severe than that for the transverse field. This is consistent with the observation, which measures the line-of-sight component much more precisely than the transverse field, and thus we have more freedom to modify the transverse field. Still, it should be noted that here the potential-field model B_z may not approximate the real chromospheric B_z well, which is preferred to be taken by direct measurements, if available.

We finally show in Figure 7 the iteration process in the optimization method. Only the result for AR 11283 is plotted as an example. As shown, the functional L decreased very quickly. After only 200 iteration steps, it almost reached its minimum, reduced by about two orders of magnitude from its initial value. The sub-functionals L_1 and L_2 show a similar

evolution, although with small oscillations, and the sub-functional L_4 continually decreases, but very slowly after 200 steps.

5. Conclusions

We have developed a new code of preprocessing the photospheric vector magnetograms for NLFFF extrapolation. The method is based on the simple rule that any vector magnetogram can be split into a potential-field part and a non-potential part, and we dealt with the two parts separately. Preprocessing the potential part was simply performed by taking the data sliced at a plane about 400 km above the photosphere from the 3D potential-field numerical solution, which was extrapolated from the observed vertical field. Then the non-potential part was modified by an optimization method to fulfill the constraints of total magnetic force-freeness and torque-freeness. For the practical computation based on numerical discretization, a strict satisfaction of force-free constraints is apparently not necessary. The extent of the smoothing to be applied to the data needs to be carefully determined as well if we aim to mimic the field expansion from the photosphere to some specific height above. We used the values of force-freeness and smoothness calculated from the preprocessed potential-field part as a reference to guide the preprocessing of the non-potential field part, *i.e.*, we required that the target magnetograms have the same level of force-freeness and smoothness as the reference data. These requirements can restrict the values of the free parameters well, *i.e.*, the weighting factors in the optimization functional. The code was applied to SDO/HMI data. The preprocessed results showed that the method can efficiently remove the force and noise if we choose the weighting factors properly. For two sampled HMI magnetograms, we found that the optimal weights are $\mu_3 = 0.001$ and $\mu_4 = 1$, with which the target magnetograms can be driven to be force-free and smooth with the same level as that of the numerical potential field at the bottom of the force-free domain.

The preprocessing code here was developed as a sub-program for a project of applying our extrapolation code CESE–MHD–NLFFF (Jiang, Feng, and Xiang, 2012; Jiang and Feng, 2012a) to observed data. We applied CESE–MHD–NLFFF to SDO/HMI data with both raw and preprocessed magnetograms (Jiang and Feng, 2013). By a careful comparison of the results, we found that the quality of extrapolation is indeed improved using the preprocessed magnetograms, including the force-freeness of the results (*e.g.*, measured by a current-weighted mean angle between the magnetic field **B** and electric current **J**) and the free-energy contents. For example, in the extrapolation of AR 11283, the mean angle between **B** and **J** for the entire extrapolation box of $600 \times 512 \times 300$ pixels was reduced from 24° to 17° and the free energy was increased from $\approx 0.5 \times 10^{32}$ erg to 1.0×10^{32} erg.

Acknowledgements This work is jointly supported by the 973 program under grant 2012CB825601, the Chinese Academy of Sciences (KZZD-EW-01-4), the National Natural Science Foundation of China (41204126, 41274192, 41031066, and 41074122), and the Specialized Research Fund for State Key Laboratories. Data are courtesy of NASA/SDO and the HMI science teams. The authors thank the anonymous referee for invaluable comments.

References

Aly, J.J.: 1989, *Solar Phys.* **120**, 19.
Amari, T., Boulmezaoud, T.Z., Aly, J.J.: 2006, *Astron. Astrophys.* **446**, 691.
Amari, T., Aly, J.J., Luciani, J.F., Boulmezaoud, T.Z., Mikic, Z.: 1997, *Solar Phys.* **174**, 129.

Aschwanden, M.J., Wuelser, J.P., Nitta, N.V., Lemen, J.R., DeRosa, M.L., Malanushenko, A.: 2012, *Astrophys. J.* **756**, 124.
Bobra, M.G., van Ballegooijen, A.A., DeLuca, E.E.: 2008, *Astrophys. J.* **672**, 1209.
Borrero, J., Tomczyk, S., Kubo, M., Socas-Navarro, H., Schou, J., Couvidat, S., Bogart, R.: 2011, *Solar Phys.* **273**, 267.
DeRosa, M.L., Schrijver, C.J., Barnes, G., Leka, K.D., Lites, B.W., Aschwanden, M.J. *et al.*: 2009, *Astrophys. J.* **696**, 1780.
Fuhrmann, M., Seehafer, N., Valori, G.: 2007, *Astron. Astrophys.* **476**, 349.
Fuhrmann, M., Seehafer, N., Valori, G., Wiegelmann, T.: 2011, *Astron. Astrophys.* **526**, A70.
Gary, G.A.: 2001, *Solar Phys.* **203**, 71.
Inoue, S., Kusano, K., Magara, T., Shiota, D., Yamamoto, T.T.: 2011, *Astrophys. J.* **738**, 161.
Jiang, C., Feng, X., Xiang, C.: 2012, *Astrophys. J.* **755**, 62.
Jiang, C.W., Feng, X.S.: 2012, *Astrophys. J.* **749**, 135.
Jiang, C.W., Feng, X.S.: 2012, *Solar Phys.* **281**, 621.
Jiang, C.W., Feng, X.S.: 2013, *Astrophys. J.* **769**, 144.
Leka, K., Barnes, G., Crouch, A., Metcalf, T., Gary, G., Jing, J., Liu, Y.: 2009, *Solar Phys.* **260**, 83.
Liu, S., Su, J.T., Zhang, H.Q., Deng, Y.Y., Gao, Y., Yang, X., Mao, X.J.: 2013, *Publ. Astron. Soc. Aust.* **30**, e005. doi:10.1017/pasa.2012.005, ADS:2013PASA...30....5L.
McClymont, A.N., Jiao, L., Mikic, Z.: 1997, *Solar Phys.* **174**, 191.
Metcalf, T.R., Jiao, L., McClymont, A.N., Canfield, R.C., Uitenbroek, H.: 1995, *Astrophys. J.* **439**, 474.
Metcalf, T.R., DeRosa, M.L., Schrijver, C.J., Barnes, G., van Ballegooijen, A.A., Wiegelmann, T., Wheatland, M.S., Valori, G., McTtiernan, J.M.: 2008, *Solar Phys.* **247**, 269.
Press, W.H., Teukolsky, S.A., Vetterling, W.T., Flannery, B.P.: 1992, *Numerical Recipes in FORTRAN. The Art of Scientific Computing*, Cambridge University Press, Cambridge, 414.
Sakurai, T.: 1989, *Space Sci. Rev.* **51**, 11.
Su, Y., van Ballegooijen, A., Lites, B.W., Deluca, E.E., Golub, L., Grigis, P.C., Huang, G., Ji, H.: 2009, *Astrophys. J.* **691**, 105.
Tadesse, T.: 2011, Nonlinear force-free reconstruction of the coronal magnetic field with advanced numerical methods, Ph.D. thesis, Max Planck Institute for Solar System Research.
Turmon, M., Jones, H.P., Malanushenko, O.V., Pap, J.M.: 2010, *Solar Phys.* **262**, 277.
Valori, G., Kliem, B., Fuhrmann, M.: 2007, *Solar Phys.* **245**, 263.
Wheatland, M.S., Sturrock, P.A., Roumeliotis, G.: 2000, *Astrophys. J.* **540**, 1150.
Wiegelmann, T.: 2004, *Solar Phys.* **219**, 87.
Wiegelmann, T.: 2008, *J. Geophys. Res.* **113**, 3.
Wiegelmann, T., Inhester, B., Sakurai, T.: 2006, *Solar Phys.* **233**, 215.
Wiegelmann, T., Neukirch, T.: 2006, *Astron. Astrophys.* **457**, 1053.
Yamamoto, T.T., Kusano, K.: 2012, *Astrophys. J.* **752**, 126.